Temperature dependence of structural and luminescence properties of Eu3+-doped Y2O3 red-emitting phosphor thin films by pulsed laser deposition

3 authors:

Abdub Guyo Ali
University of the Free State
6 PUBLICATIONS   19 CITATIONS

SEE PROFILE

Francis Dejene
University of the Free State
25 PUBLICATIONS   85 CITATIONS

SEE PROFILE

H. C. Swart
University of the Free State
528 PUBLICATIONS   3,327 CITATIONS

SEE PROFILE

Applied Physics A
Materials Science & Processing

CrossMark

Temperature dependence of structural and luminescence properties of Eu^{3+}-doped Y$_2$O$_3$ red-emitting phosphor thin films by pulsed laser deposition

A. G. Ali[1] · B. F. Dejene[1] · H. C. Swart[2]

Abstract Pulse laser deposition was used to obtain nanocrystalline red-emitting Y$_2$O$_3$:Eu^{3+} thin-film phosphors. X-ray diffraction measurements show that the un-annealed thin film was amorphous, while those annealed were crystalline. At lower annealing temperature of 600–700 °C, cubic bixbyite Y$_2$O$_3$:Eu^{3+} was formed. As the annealing temperatures were increased to 800 °C, hexagonal phase emerged. The average crystallite size of the film was 64 nm. Photoluminescence measurement indicates intense red emission around 612 nm due to the ^{5}D$_0$ → ^{7}F$_2$ transition. Scanning electron microscopy indicated that agglomerates of non-crystalline particles with spherical shapes were present for the un-annealed films. After annealing at high temperature, finer morphology was revealed. Atomic force microscopy further confirmed the formation of new morphology at the higher annealing temperatures. UV–Vis measurement indicated a band gap in the range of 4.6–4.8 eV. It was concluded that the annealing temperature played an important role in the luminescence intensity and crystallinity of these films.

1 Introduction

In an early development of low-voltage cathodoluminescent (CL) phosphors for applications in field emission display (FED) devices, the cathode-ray tube (CRT) phosphors have readily been tested as candidates. In the case of the red phosphor materials, unfortunately, Y$_2$O$_2$S:Eu^{3+} which is used as the red primary colour in the CRT has known to be degraded under electron bombardments with high current densities and the sulphur containing volatile gases escaping from the surface under electron bombardment contaminate the cold cathodes, resulting in a fatal damage to FED devices [1]. The oxide-based thin-film phosphors are highly attractive in the use of the FED devices because of the advantages such as higher lateral resolution from smaller grains, better thermal and mechanical stability, and reduced outgassing over conventional powder phosphors [2]. Among the oxide phosphors, Y$_2$O$_3$:Eu^{3+} is currently one of the leading red phosphor materials for FEDs [3]. Y$_2$O$_3$:Eu^{3+} films have been grown using various deposition techniques [4–6]. However, because of its high melting point of about 2400 °C, Y$_2$O$_3$:Eu^{3+} thin films require a post-annealing process at high temperatures above 1000 °C to crystallize the deposits [7–10]. Therefore, the high-temperature process is inevitable in order to obtain high efficient and bright Y$_2$O$_3$:Eu^{3+} thin-film phosphors and Y$_2$O$_3$:Eu^{3+} films had been grown only on the heat-resistant substrates such as Si wafers [11, 12], Ni-based alloys [13] and sapphire plates [14, 15]. However, annealing at high temperature is definitely a concern for the fabrication of the current FED devices which adapt low-temperature glass substrates. By replacing the rastered electron beams in the CRT with an array of cathodes, FEDs promise to be significantly thinner and lighter have higher brightness, better power efficiency and viewing angle, and operate over a large temperature range as compared to liquid crystal displays (LCDs) [16–18]. While the cathode array enables FEDs, the light from this emissive display comes from the phosphor anode. Phosphor anodes are currently powders screened onto glass

✉ A. G. Ali
  aliag@ufs.ac.za

1 Department of Physics, University of the Free State (Qwaqwa Campus), Private Bag X13, Phuthaditjhaba 9866, South Africa

2 Department of Physics, University of the Free State, P.O. Box 339, Bloemfontein 9300, South Africa

Springer

plates using a variety of techniques including electrophoretic, dusting and slurry methods [19]. The slurry method is the most common method, in which phosphor powder is mixed with photosensitive chemicals and is patterned using photolithography techniques. For operating voltages greater than 2 kV, the screen is back coated with a thin layer of aluminium which acts as an optical reflector as well as a charge dissipater [20–22]. At operating voltage below 2 kV, the electron penetration depth is so small that the screens are left un-coated [23–25]. Even though powder phosphors are very efficient, the particle size may limit resolution of the display. Thin films are an alternative to powder phosphors and have both advantages and disadvantages as compared to powders [26]. Pulse laser deposition (PLD) offers many advantages over other film deposition techniques such as chemical vapour deposition (CVD) or physical vapour deposition (PVD). Unlike the CVD process in which complicated precursors are used as starting materials, PLD uses a pre-pressed solid target from which the thin-film structure is deposited by the laser ablation process. The film growth rate can be easily controlled by varying the laser parameters, background gas composition and pressure, substrate to target distance, etc. The main feature of the PLD method is the excellent stoichiometric transfer from the complex inorganic targets to the films, and the homogeneity and uniformity over the designated depositing areas [27]. A suitable phosphor must be efficiently excited by the given wavelength of the LED and must emit high luminance at a good portion of visible electromagnetic spectrum. The Eu^{3+}-doped Y_2O_3 material offers many advantages over other phosphor materials as a candidate for red-emitting applications due to its characteristic energy levels [28].

The intention of the present research is to investigate whether modifying the surface of deposited thin-film phosphors by annealing at different temperatures would result in increased efficiency. We therefore report on the study of the annealing temperature on pulsed laser deposited thin films, the consequent crystalline and surface morphology structures, and photoluminescence (PL) characteristics of Y_2O_3:Eu^{3+} thin films.

2 Experimental details

2.1 Powder synthesis

Y_2O_3:Eu^{3+} nanocrystals were synthesized using the sol-combustion route. The method of synthesis essentially comprises of mixing the precursors in appropriate stoichiometric ratios, followed by firing in an air tube furnace at a temperature of 400 °C. The white foamy product was then grounded and left to dry in an enclosed oven for 24 h.

2.2 Pulsed laser deposition (PLD)

The Si (100) wafers used as substrate were first chemically cleaned. The phosphor was pressed with binders to prepare a pellet that was used as an ablation target. The deposition chamber was evacuated to a base pressure of 8×10^{-6} mtorr. The Lambda Physic 248-nm KrF excimer laser was used to ablate the phosphor pellet in a constant 20 mtorr O_2 atmospheres. A Baratron Direct (Gas Independent) Pressure/Vacuum capacitance Manometer (1.33×10^{-2} mtorr) was used for the high-pressure measurements. The laser energy density, number of pulses and laser frequency were set to 0.74 J/cm^2, 12,000 and 10 Hz, respectively. The substrate temperature was fixed at 300 °C, and the target to substrate distance was 6 cm. The ablated area was 1 cm^2. The films were then annealed at the temperatures of 600, 700, 800 and 900 °C.

2.3 Characterization

The Shimadzu Superscan SSX-550 system was used to collect the scanning electron microscopy (SEM) micrographs. Atomic force microscopy (AFM) micrographs were obtained from the Shimadzu SPM-9600 model. X-ray diffraction (XRD) data were collected by using a SIEMENS D5000 diffractometer using CuKα radiation of $\lambda = 1.5405$ nm. PL excitation and emission spectra were recorded using a Cary Eclipse fluorescence spectrophotometer (Model: LS 55) with a built-in xenon lamp and a grating to select a suitable wavelength for excitation. The excitation wavelength was 209 nm, and the slit width was 10 nm. The afterglow curves for the films were also obtained with the Cary Eclipse spectrophotometer.

3 Results and discussions

3.1 Structural and morphological analysis

3.1.1 X-ray diffraction analysis (XRD)

XRD data were analysed for the identification of phase and crystallite size. Figure 1 shows the X-ray diffraction patterns of the un-annealed and thin films annealed at the temperature of 600–900 °C for 2 h. The un-annealed thin film was amorphous, while those annealed were crystalline. Two different phases were obtained at low and high annealing temperatures. The thin film annealed at lower temperatures were indexed to cubic bixbyite phase [space group Ia-3(206)] with average lattice constant $a = 10.60$ Å which is in good agreement with the standard value for bulk cubic Y_2O_3 (JCPDS No. 72-0927). At low annealing temperature (600–700 °C), there are mainly two diffraction
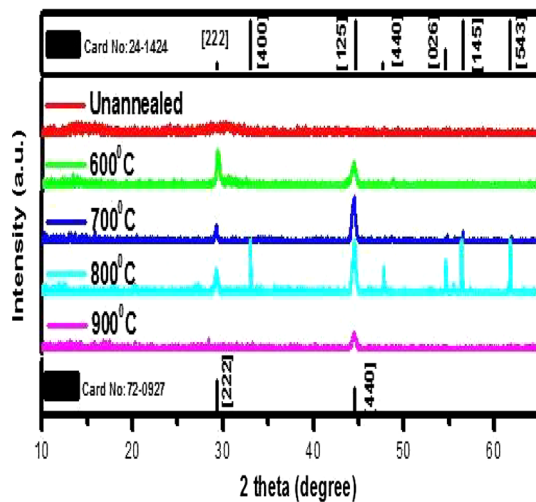
Fig. 1 X-ray diffraction pattern of un-annealed and annealed Y$_2$O$_3$: Eu^{3+} thin film deposited on a (100) Si substrate after firing at temperatures between 600 and 900 °C in air for 2 h

Fig. 2 Crystallite sizes and lattice parameters as a function of temperature

peaks at 2 theta values of 29.4 and 44.3. It can be clearly seen that by increasing the annealing temperature to 800 °C more peaks emerged at 2 theta values of 29.4, 33.0, 44.5, 47.8, 54.6, 56.3 and 62.0. This seven diffraction peaks indexed to hexagonal structure of Y$_2$O$_3$ are in agreement with data from JCPDS card No. 24-1424 with average lattice constants $a = 3.779$ and $c = 6.590$. The thin film annealed at 900 °C also revealed two peaks at 2 theta values of 29.4 and 44.5 similar to the peaks annealed at 600 and 700 °C, indicating same phase of cubic. This change in the structure when the annealing temperature is increased to 800 °C could be due to reduction in the lattice stress. The films annealed at 600, 700 and 900 °C have large lattice stress, while the stress of film at 800 °C is small. The role of crystal field change in the formation of a new phase should not be neglected as well. The broadening of the peaks in both the phases suggests small particle size. No other impurities peaks have been found which means that dopant ion completely occupies the Y$_2$O$_3$ host lattice. Also, the ionic radii of Y^{3+} (0.90Å) and Eu^{3+} (0.89 Å) are very close, and hence, it is possible to substitute Y^{3+} with Eu^{3+} ions.

Figure 2 shows the role of annealing temperature on crystallite sizes and lattice parameters. A slight increase in the crystallite size and a decrease in lattice parameters are established by means of X-ray diffraction analysis for a series of thin films annealed at temperatures between 600 and 900 °C.

Further, it is marked that as the sample is annealed at higher temperatures the FWHM (full width at half maximum) of the di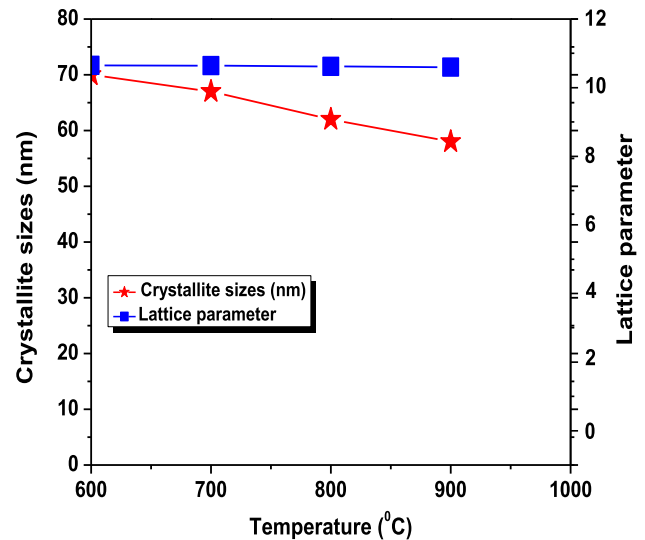ffraction peaks decreased and peaks became sharper. This suggest for an increase in the crystalline size of the annealed sample. To confirm this, crystalline size of both samples was calculated using the Scherrer formula [29].

$$D = \frac{0.9\lambda}{\beta \cos \theta}$$

where D is crystallite size, λ is the wavelength of incident X-ray [Cuk (1.54056)], β is the FWHM and θ is the diffraction angle for (hkl) plane. To calculate crystallite size, three most intense peaks (29.24°, 32.91° and 44.51°) were selected. The FWHM of these peaks were taken by their Gaussian peak fitting. The average crystallite size for the annealed films calculated through aforementioned procedure comes out to be 64 nm. The lattice parameters and crystallite sizes are shown in Table 1.

3.1.2 Scanning electron microscopy (SEM)

The morphologies of the nanostructures of the Y$_2$O$_3$: Eu^{3+} thin films were studied by the SEM patterns and are presented in Fig. 3. It shows that the obtained films are composed of particles which are nearly spherical in shape. SEM micrograph shows the aggregated nature of the secondary particles which were made up of the agglomeration of many primary particles. The films which were un-annealed and those annealed at lower temperatures appeared with the same morphology and crystalline sizes. At higher annealing temperature, the morphology of the film changed drastically to finer one probably due to change in the structure as also revealed by XRD.

Table 1 Showing lattice parameters and crystalline sizes of Y_2O_3: Eu^{3+} thin films

Annealing temp. (°C)	Lattice parameters			Crystallite size (nm)
	Hexagonal phase		Cubic phase	
	a	c	a	
Un-annealed	–	–	–	–
600	3.712	6.575	10.603	70
700	3.790	6.630	10.625	67
800	3.796	6.645	10.647	62
900	3.815	6.649	10.654	58

Fig. 3 SEM micrographs of (a) un-annealed and annealed samples, (b) 600, (c) 800 and (d) 900 °C
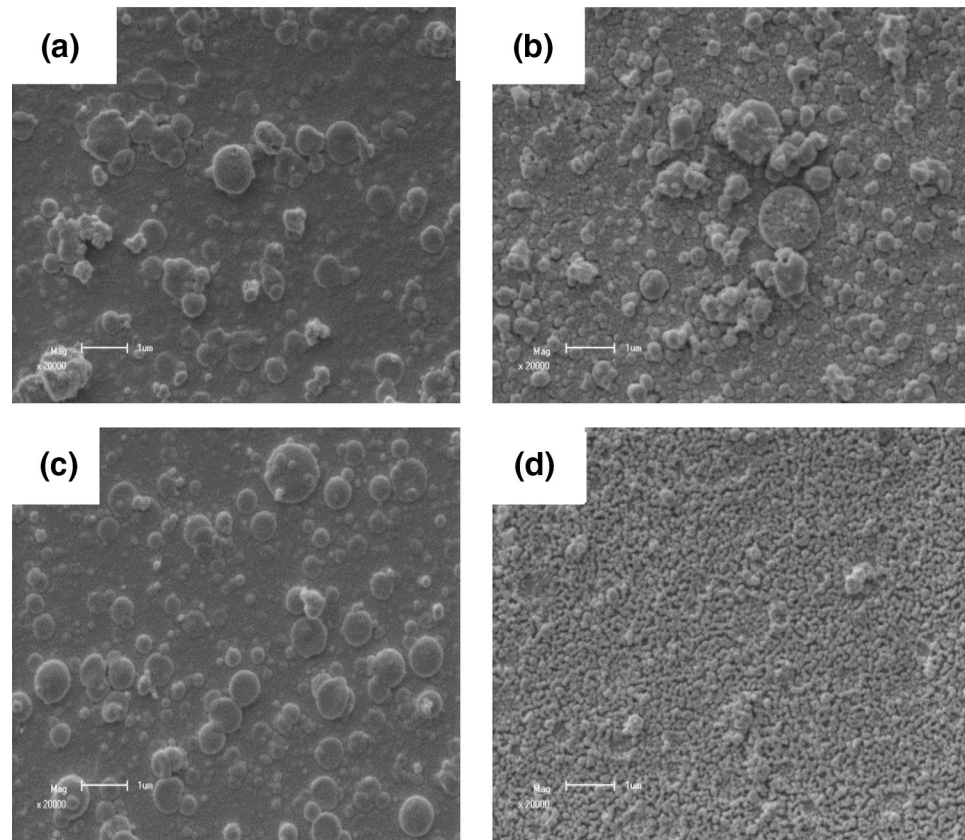
3.1.3 Atomic force microscopy

Figure 4 shows the AFM images of the Y_2O_3: Eu^{3+} thin films (a) un-annealed, (b) annealed at 600 °C and (c) annealed at 900 °C in an open-air furnace. The images were obtained in contacting mode taken over a scale of 5×5 μm^2. Better crystal gain can be obtained by annealing at different temperatures, and the surface with different features can also be observed. The crystal grains of Y_2O_3:Eu^{3+} film annealed at higher temperature is more even, and the grain size is lesser than that of un-annealed sample. The uneven grains are distributed on the surface of Y_2O_3:Eu^{3+} un-annealed film, large 72 nm and small 40 nm.

3.2 Optical properties

The UV–visible reflectance spectra of the as prepared samples are illustrated in Fig. 5. The spectra of all the samples show good optical quality in the visible range due to the complete reflectance in the 200–400 nm range. It clearly indicates that the percentage reflectance is significantly affected by the annealing temperature. The materials also reflect significantly in the UV region as compared to visible region. From the graph, Fig. 5, the material reflects between 320 and 350 nm depending on the annealing temperatures. Except for the thin film annealed at 900 °C, the wavelength of the films increased with increasing annealing temperature. Furthermore, absorption bands
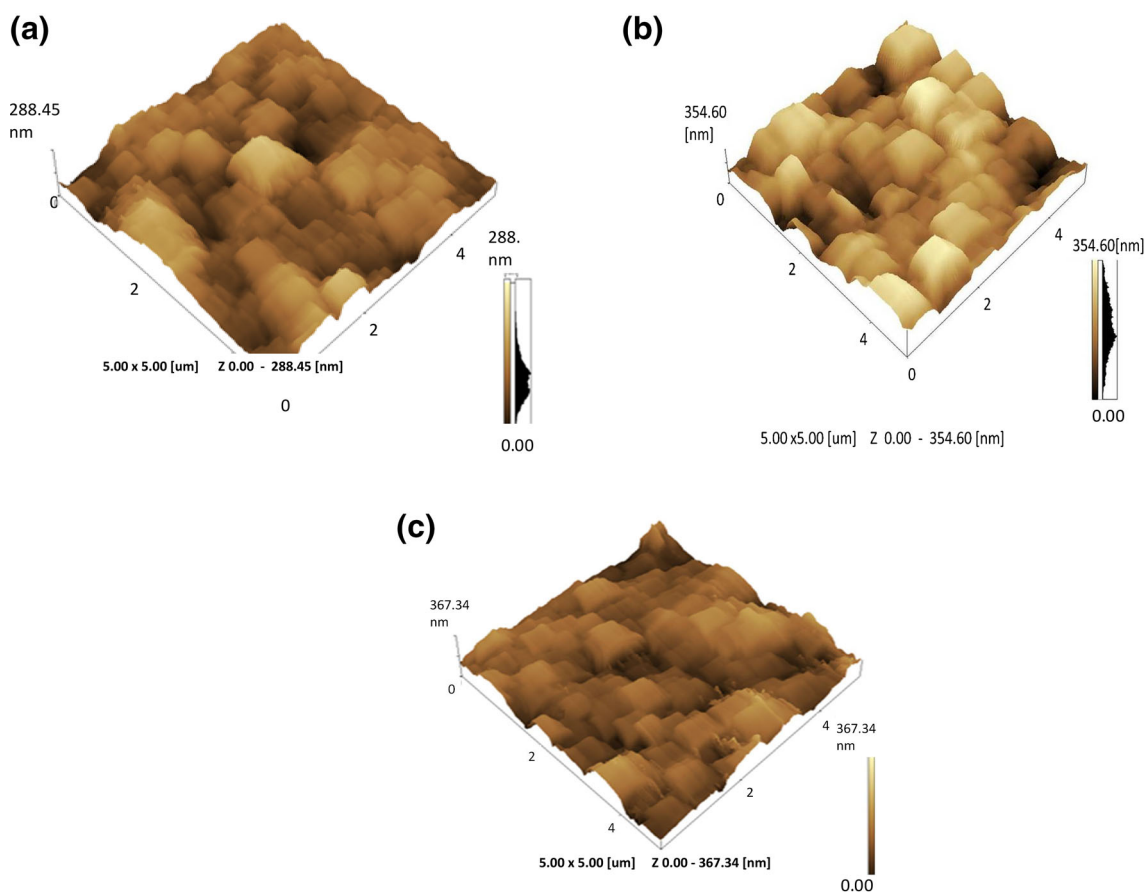
(a)

(b)

(c)

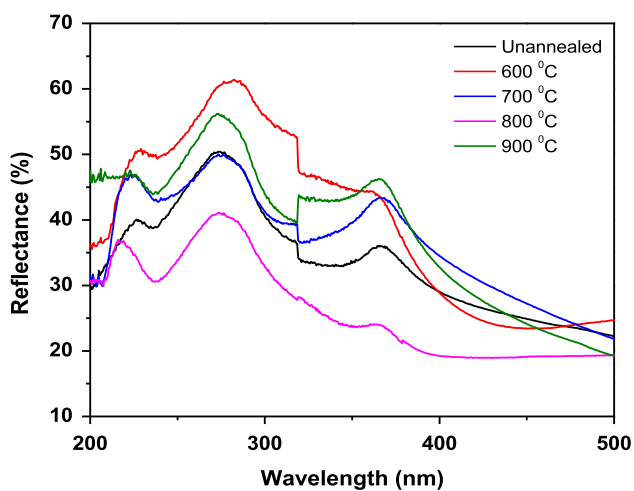Fig. 4 3D height AFM images done in contact mode for the thin films **a** un-annealed, **b** annealed at 600 and **c** annealed at 900 °C

Fig. 5 Diffuse reflectance measurements for un-annealed and those annealed at different temperatures for Y2O3:Eu^{3+} thin films
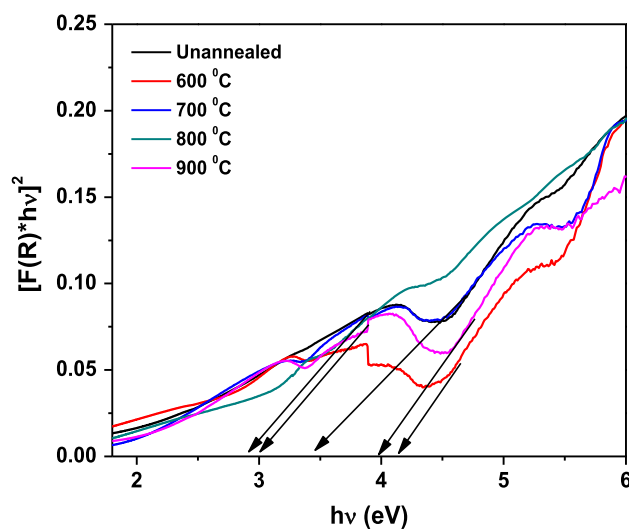
Fig. 6 Graph of F[(R) * hv]^2 as a function of band gap energy

corresponding to the forbidden 4f–4f transitions are usually weak and therefore not detected [30].

Figure 6 shows graph of $[F(R) * hv]^2$ versus hv for the un-annealed and thin films annealed at various temperatures. In order to calculate the band gap of the films, the following Kubelka–Munk equation was used;

$$F(R_\infty) = (1 - R_\infty)^2/2R_\infty = K/S \qquad (1)$$

where $R_\infty = R_{sample}/R_{references}$, K is absorption coefficient and S is scattering coefficient.

On the other hand, the bang gap E_g and absorption coefficient α of direct band gap semiconductor are related through the well-known Tauc relation:

$$\alpha h\nu = C_1 (h\nu - E_g)^{1/2} \qquad (2)$$

where $h\nu$ is the photo-energy and C_1 is proportionality constant. When the material scatters in a perfectly manner, the absorption coefficient K becomes equal to 2α ($K = 2\alpha$). Considering the scattering coefficient S as constant with respect to wavelength, and using Eqs. (1) and (2), the following expression can be written as:

$$[F(R_\infty) * h\nu]^2 = C_2(h\nu - Eg) \qquad (3)$$

By plotting $[F(R) * h\nu]^2$ against $h\nu$ and fit the linear region with a line and extend it to the energy axis, then one can easily obtain E_g by extrapolating the linear regions to $[F(R_\infty)h\nu]^2 = 0$. The arrows in the figure indicate these extrapolations for the un-annealed and the thin films annealed at different temperatures. E_g is the band gap at $n = 2$ for direct transitions. From the figure, the band gap of Y_2O_3: Eu^{3+} was found to be in the range of 2.9–4.3 eV. It can be seen clearly that the band gap energy of the Y_2O_3 decreases linearly with increasing temperature. The presences of two or more slopes suggest that the samples have some impurities.

3.3 Photoluminescence

3.3.1 Excitation spectra

Figure 7 gives the PL excitation spectra of the Y_2O_3:Eu^{3+} thin films for un-annealed and those films annealed at temperatures between 600 and 900 °C. These spectra consist of several excitation bands which are ascribed to different transitions. In the excitation spectrum monitored by $^5D_0$–$^7F_2$ transition of Eu^{3+} at 612 nm for Y_2O_3:Eu^{3+} thin films, the broad band with a maximum at 209 nm originates from the excitation of the oxygen-to-europium ($O^{2-} \rightarrow Eu^{3+}$) charge transfer band (CTB) and some very weak peaks in the longer-wavelength region of 300 nm are ascribed to the $f \rightarrow f$ transitions of the Eu^{3+} ions. The band located at 234 nm is due to host absorption band.

3.3.2 Emission spectra

Figure 8 shows the emission spectra of un-annealed and films annealed between 600 and 900 °C. The emission spectra were recorded at excitation wavelength of 209 nm. The decrease in the PL intensity with the increase in annealing temperature can be attributed to rougher surfaces
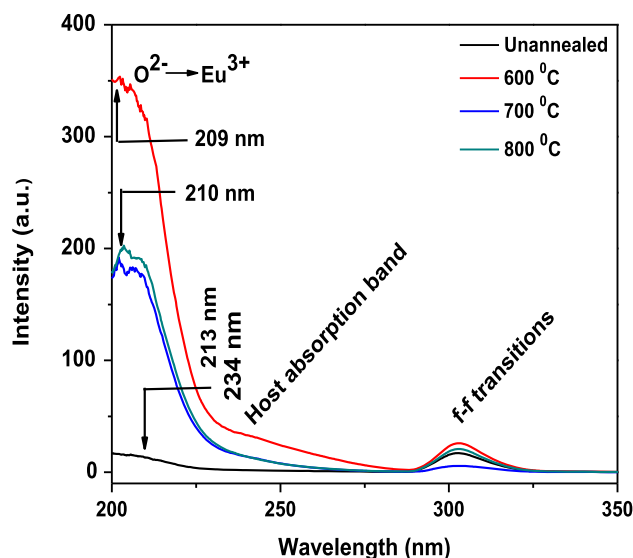

Fig. 7 Excitation spectrum of Y_2O_3: Eu^{3+} thin films for un-annealed and those annealed at 600, 700 and 800 °C

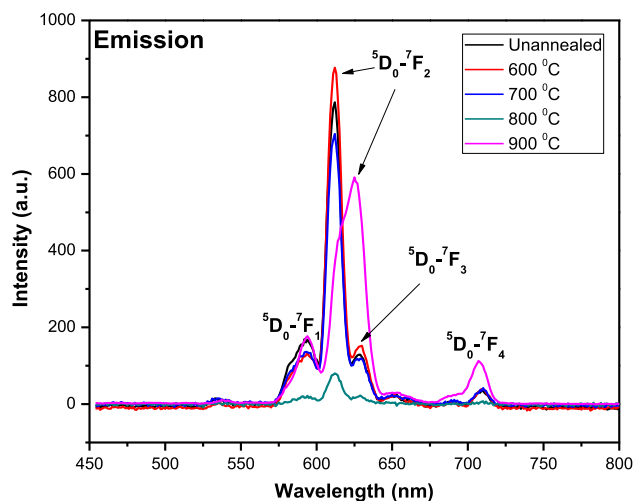**Fig. 8** Emission spectrum of Y_2O_3: Eu^{3+} thin films for un-annealed and those annealed at 600, 700, 800 and 900 °C

and improved optical properties of larger crystallite sizes for as-deposited film. It is well known that rough surfaces increase the probability of light emission from the surface by limiting the chances of total internal reflection at the film–substrate interface [31]. This relative decrease in the PL intensity with the annealing temperature suggests the decrease in the grains which plays a major role in increasing defect densities. Similar behaviour was observed by Mckittrick et al. [32], in their study of characterization of photoluminescent $(Y_{1-x}Eu_x)_2O_3$ thin films prepared by metallorganic chemical vapour deposition. The most intense peaks appearing at 612 nm are recorded for the un-annealed and films annealed at lower temperatures

of 600 and 700 °C. At higher annealing temperature of 800 °C, this peak is tremendously quenched possibly due to structural change. At annealing temperature of 900 °C, all these peaks are quenched, but the peak appearing at 612 nm is red-shifted and enhanced which is a confirmation of formation of a new phase. Also, this peak is predominant at 588- and 715-nm wavelengths. This phenomenon can be explained by the fact that the 209-nm radiation excites the Eu^{3+} ions from ground state to the higher excited state $^5D_0$–$^7F_2$ and quickly relaxes to $^5D_0$–$^7F_4$ level by emitting non-radiative transition. The strong red emission band centred at 612 nm corresponds to the hypersensitive transition $^5D_0$–$^7F_2$. Another feeble yellow emission band at 588 nm corresponds to $^5D_0$–$^7F_1$ transition, which is less sensitive to the host. The reason behind observing the intense red emission from Y$_2$O$_3$:Eu^{3+} can be understood by considering the structure of Y$_2$O$_3$. The coordinate number of Y$_2$O$_3$ is six and forms cubic bixbyite structure with two different sites (C_2 and S_6) for RE ions substitution. The C_2 is a low symmetry site without an inversion centre, whereas C_2 is a high symmetry site having an inversion centre. When Eu^{3+} is located at a low symmetry (C_2), the red emission is dominant, whereas the yellow emission is dominant when Eu^{3+} is located at high symmetry (S_6) [33, 34]. In the present case, red emission is dominant suggesting that the location of Eu^{3+} is more favourable at C_2 site. As the C_2 site does not have an inversion centre, electric dipole transition from Eu^{3+} ions attached to this site is more favourable than the magnetic dipole transitions. The similarity of the ionic radii of Eu^{3+} and Y^{3+} ions allows the easy substitution of Y^{3+} ions with Eu^{3+} ions at C_2 sites giving rise to intense red emission in the un-annealed and films annealed at lower temperatures [35].

Figure 9 represents the chromaticity coordinates of the PL spectra for the samples (a) un-annealed and those annealed at (b) 600, (c) 700, (d) 800 and (e) 900 °C, which are determined using the CIE (International Commission on Illumination) Coordinate Calculator software. According to the software, the position of the colour coordinates lie well in the red and orange region. The detailed analysis of the phosphor finds its suitability in making the red/orange producing phosphor for display applications and light emitting diodes.

3.3.3 Decay curve

Figure 10 shows the decay characteristics of the thin films un-annealed and those annealed at temperatures between 600 and 900 °C. The films which are un-annealed and those annealed at lower temperatures have the highest initial intensities. This is also consistent with the PL spectra shown in Fig. 8. The films were characterized by
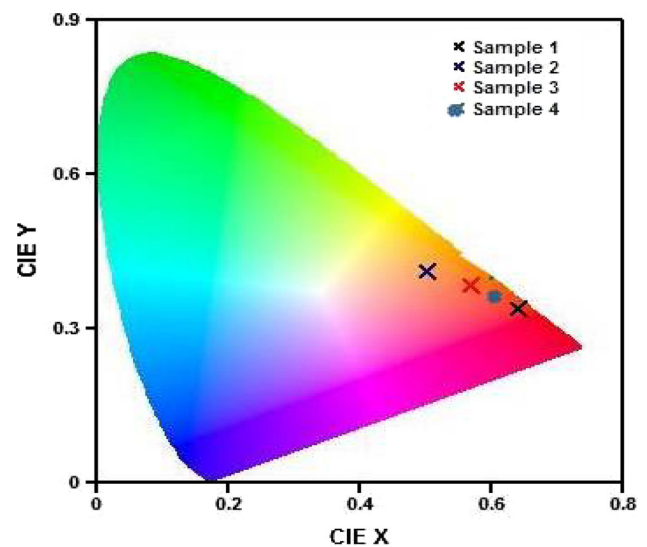

Fig. 9 CIE coordinates for samples that were un-annealed and those annealed at various temperatures
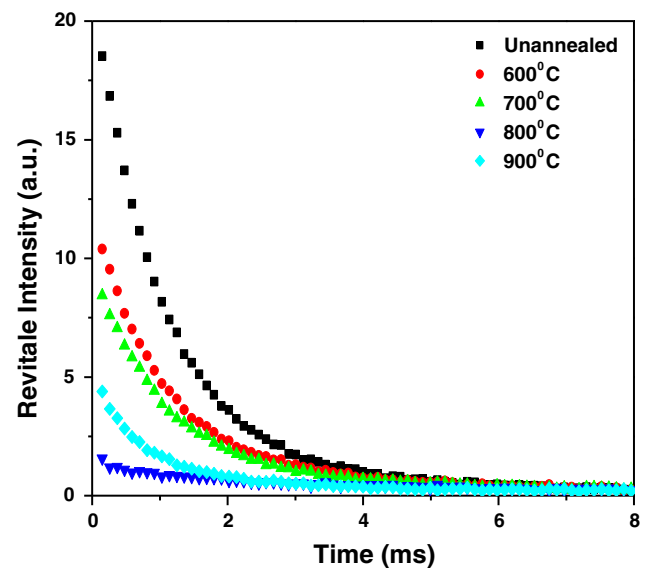

Fig. 10 Showing decay characteristics of Y$_2$O$_3$: Eu^{3+} phosphor thin films for un-annealed and films annealed at 600, 700, 800 and 900 °C

the fast and medium decays characteristics, since they are indicative of the different rates of decay for the films. The decay curves were fitted according to Eq. (4) and gave the decay constants listed in Table 2.

$$I = A_1 \exp\left(-t/\tau_1\right) + A_2 \exp\left(-t/\tau_2\right) \qquad (4)$$

where I is phosphorescence intensity, A_1 and A_2 are constants, t is time and τ_1 and τ_2 are decay constants, deciding the decay rate for rapid and slow exponentially decay components, respectively. The fitting results of parameters τ_1 and τ_2 are listed in Table 2.

Table 2 Results for the fitted decay curves of the un-annealed and films annealed at different temperatures

Temperature (°C)	Un-annealed	600	700	800	900
Components					
Fast (τ_1)	0.5896	0.5524	0.5275	0.5165	0.4962
Medium (τ_2)	0.8564	0.8124	0.7856	0.7522	0.7050

Two components, namely fast and slow, are responsible for the luminescence properties of the as-synthesized phosphor. A trend can be observed (Table 2) that the decay constants of the phosphors decrease gradually with the increasing annealing temperature.

4 Conclusion

Highly luminescent red nanophosphors of Eu^{3+}-doped Y_2O_3 were fabricated by using PLD. XRD confirmed that the un-annealed thin films were amorphous. The annealed films reveal cubic phase when annealed at 600, 700 and 900 °C but hexagonal phase at 800 °C. The average crystallite size of the films after annealing was 64 nm. SEM images show similar morphology for the un-annealed and films annealed at lower temperatures which changed at higher temperature. AFM shows that the crystal grains of Y_2O_3:Eu^{3+} films annealed at higher temperature are uniform and the grain size is smaller than that of un-annealed sample. PL shows that the most intense red luminescence corresponding to $^5D_0$–$^7F_2$ transition of Eu^{3+} appearing at 612 nm is recorded for the un-annealed and films annealed at lower temperatures of 600 and 700 °C. At higher annealing temperature of 800 °C, this peak is tremendously quenched possibly due to structural change. At annealing temperature of 900 °C, all these peaks are quenched, but the peak appearing at 612 nm is red-shifted and enhanced. Also, this peak is predominant at 588- and 715-nm wavelengths. The decrease in the PL intensity with the increase in annealing temperature can be attributed to rougher surfaces and improved optical properties of larger crystallite sizes for un-annealed film. UV–Vis measurement indicated a band gap in the range of 2.9–4.3 eV. This provides a general deposition method for rare-earth-doped oxide nanocrystals with potential applications such as high-definition displays.

References

1. H.C. Swart, J.C. Sebastian, T.A. Trottier, S.R. Jones, P.H. Holloway, J. Vac. Sci. Technol., A **13**, 1697 (1996)
2. G.A. Hirata, J. Mckittrick, M. Avalos-Borja, J.M. Siqueiros, D. Devlin, Appl. Surf. Sci. **113**, 509 (1997)
3. S.L. Jones, D. Kumar, K.G. Cho, R. Singh, P.H. Holloway, Displays **19**, 151 (1999)
4. R.N. Sharma, S.T. Lakshami, A.C. Rastogi, Thin Solid Films **199**, 1 (1991)
5. K. Onisawa, M. Fuyama, K. Tamura, K. Taguchi, T. Nakayama, Y. Ono, J. Appl. Phys. **66**, 719 (1990)
6. R. Rao, Solid State Commun. **99**, 439 (1996)
7. K.L. Choy, J.P. Feistand, A.L. Heys, B. Su, J. Mat. Res. **14**, 3111 (1999)
8. S.L. Jones, O. Kumar, R.K. Singh, P.H. Holloway, Appl. Phys. Lett. **71**, 404 (1997)
9. K.G. Cho, D. Kumar, D.G. Lee, S.L. Jones, P.H. Hollway, R.K. Singh, Appl. Phys. Lett. **71**, 3335 (1997)
10. K.G. Cho, D. Kumar, P.H. Holloway, R.K. Singh, Appl. Phys. Lett. **73**, 3058 (1998)
11. H. Leverenz, *An Introduction to Luminescence of Solids* (Dover Publications Inc, New York, 1968)
12. P.H. Holloway, S.L. Jones, P. Rack, J. Sebastian, T. Trottier, in *Proceedings of 10th International Symposium Applications of Ferroelectrics*, ed. by B. Kulwicki (East Brunswick, NJ, (IEEE, NY,) 1996), p. 127
13. T. Hase, T. Kano, E. Nakazawa, E. Yamamoto, E. Adv. Electron. Electron Phys. **79**, 11–19 (1990)
14. H. Bechtel, W. Czarnojan, M. Haase, W. Mayr, H. Nikol, Philips J. Res. **50**, 433 (1996)
15. C.M. Feldman, J. Opt. Soc. Am. **47**, 790 (1957)
16. M.R. Royce, US Patent no. 3418, vol. 246 (1968)
17. S.H. Cho, Y.S. Yoo, J.D. Lee, J. Electrochem. Soc. **145**, 1017 (1998)
18. T. Matsuzawa, Y. Aoki, N. Takeuchi et al., A new long phosphorescent phosphor SrA1204: Eu$^{2+''}$, Dy^{3+} with high brightness. J. Electrochem. Soc. **143**, 2670 (1996)
19. J. Qiu, M. Kawasak, K. Tanaki et al., Phenomenon and mechanism of long lasting phosphor escence in Ed'$^{2+}$-doped aluminosilicate glasses. J. Phys. Chem. Solids **59**, 1521 (1998)
20. T. Katsumata, T. Nabae, K. Sasajima, Growth and characteristics of long persistent SrA1204 and CaA1204 based phosphor crystals by a floating zone technique. J. Cryst. Growth **83**, 361 (1998)
21. T. Kinoshita, M. Yamazaki, H. Kawazoe et al., Long phosphorescence and photostimulated luminescence in Tb ion activated reduced calcium aluminate glasses. J. Appl. Phys. **86**, 3729 (1999)
22. N. Kodama, T. Takahashi, M. Yamaga et al., Long lasting phosphorescence in Ce3+ doped CaZAlzSiO7 and CaYA130 crystals. Appl. Phys. Ltt. **75**, 1715 (1999)
23. R. Sakai, T. Katsumata, S. Komuro et al., Effect of composition on the phosphorescence from BaAlzOI: Eu'', Dy3$'$ crystals. J. Lumin. **85**, 149 (1999)
24. Y.L. Chang, H.I. Hsiang, M.T. Liang, J. Alloys Comp. **461**, 598 (2008)
25. T. Peng, L. Huajun, H.J. Yang, Mater. Chem. Phys. **85**, 68 (2004)
26. P.D. Sarkisov, N.V. Popovich, A.G. Zhelnin, Glass Ceram. **60**, 9 (2003)
27. T. Peng, H. Yang, X. Pu, B. Hu, Z. Jian, C. Yan, Mater. Lett. **58**, 352 (2004)
28. X. Li, Y. Qu, X. Xie, Z. Wang, R. Li, Mater. Lett. **60**, 3673 (2006)
29. J.S. Bae, K.S. Shim, S.B. Kim, J.H. Jeong, S.S. Yi, J.C. Park, J. Cryst. Growth **264**, 290 (2004)

30. D.P. Norton, Mater. Sci. Eng., R **43**, 139 (2004)
31. S.L. Jones, D. Kumar, R.K. Singh, P.H. Holloway, Appl. Phys. Lett. **71**, 404 (1997)
32. J. McKittrick, C.F. Bacalski, G.A. Hirata, K.M. Hubbard, S.G. Pattillo, K.V. Salazar, D.M. Trkula, J. Am. Ceram. Soc. **83**, 1241 (2000)
33. D.R. Baer, A.S. Lea, J.D. Geller, J.S. Hammond, L. Koyer, C.J. Powell, M.P. Seah, M. Suzuki, J.F. Watts, J.J. Wolstenholme, Electron Spectros. Relat. Phenom. **176**, 80 (2010)
34. F. Adams, L. Van Vaeck, R. Barrett, Spectrochimica Acta Part B **60**, 13 (2005)
35. S. Choopun, H. Tabata, T. Kawai, J. Cryst. Growth **274**, 167 (2005)